

Dry Synthesis of Nanoporous Metallic Films

Hyunah Kwon ¹, Hannah-Noa Barad ¹, Alex Ricardo Silva Olaya ², Mariana Alarcon-Correa ¹, Kersten Hahn ³, Gunther Richter ¹, Gunther Wittstock ², Peer Fischer ^{1,4,*}

¹ Max Planck Institute for Intelligent Systems, Heisenbergstrasse 3, 70569 Stuttgart, Germany

² School of Mathematics and Science, Department of Chemistry, Carl von Ossietzky University of Oldenburg, 26111 Oldenburg, Germany

³ Max Planck Institute for Solid State Research, Heisenbergstrasse 1, 70569 Stuttgart, Germany

⁴ Institute of Physical Chemistry, University of Stuttgart, Pfaffenwaldring 55, 70569 Stuttgart, Germany

Abstract

Nanoporous metals possess unique properties attributed to their high surface area and interconnected nanoscale ligaments. They are mostly fabricated by wet synthetic methods involving solution-based dealloying processes whose purity is compromised by residual amounts of the less noble metal. Here, we demonstrate a novel dry synthesis method to produce nanoporous metals, which is based on the plasma treatment of metal nanoparticles formed by physical vapor deposition. Our approach is general and can be applied to many metals including non-noble ones. The resultant nanoporous metallic films are impurity-free and possess highly curved ligaments and nanopores. The metal films are remarkably robust with many catalytically active sites, which is highly promising for electrocatalytic applications.

Nanoporous metals (NPMs) exhibit unique properties distinct from the bulk.¹ The nanoscale pore-architecture directly determines the optical,² electrical,³ chemical,⁴ and mechanical⁵ properties. The high surface-area-to-volume ratios and large number density of high surface energy atoms at curved surfaces give rise to significant catalytic activities that are absent in the bulk metal.^{6,7} NPMs are also lightweight and can be optically transparent.^{8,9} Interconnected films of NPMs have thus attracted strong interest for applications as electrode materials for synthesis,¹⁰ energy conversion¹¹ and sensing,¹² or as plasmonic materials.¹³ Since NPMs do not occur naturally, they need to be synthesized.

A number of different schemes to synthesize NPMs have been developed.¹⁴⁻¹⁷ A few studies report the deposition of metals onto pre-formed inorganic or polymeric nanoporous templates, typically by electrochemical deposition or sputtering, followed by an etching step that removes the sacrificial porous support structure.¹⁸⁻²¹ However, the requirement of a separate template and multiple fabrication steps is a disadvantage. A wet-chemical sol-gel scheme has also been reported that relies on the reduction of metal salts to form metal nanoparticles followed by their aggregation.^{8,15} While it affords some freedom to vary the composition, the resulting network shows few highly curved nanoporous features and thus few grain boundaries and defect sites at the surface.²² Highly curved nanoporous features are desirable, as they support low-coordinated atoms that are favorable sites for catalytic activity.²³ By far, the most widely used method to synthesize NPMs is dealloying as it can yield reactive metallic films with higher reactivity than the flat homologue. Dealloying involves the selective chemical etching of one or more less noble metals out of an alloy.^{14,24,25} For instance, nanoporous Au structures are generally formed by etching silver out of Ag-Au alloys.²⁶ While the method is relatively simple and effective, the less noble metal, here Ag, cannot be completely removed for thermodynamic reasons. The remaining content of the less noble element is difficult to precisely control and may greatly affect the catalytic activity of the resulting NPM.^{27,28} For brevity we call this remaining content of the less noble metal “impurity” of the resulting NPM. Another challenge is that the dealloying process to form NPMs with non-noble metals requires carefully chosen combinations of materials and chemistries, so that the metals in the master alloy can be selectively etched. Generalizing the fabrication conditions using a wet synthesis is thus challenging.^{29,30} It is therefore desirable to develop a scheme that permits catalytically active NPMs to be formed from a number of metals, including non-noble metals, and free from impurities.

Here, we demonstrate a scheme to obtain impurity-free NPM films with highly curved pore structures of adjustable sizes. The NPMs are formed by the coalescence of metal nanoparticles in a low-temperature plasma. No solution-processing or harsh chemicals are required, and the process can be generally applied. We form nanoporous Au, Ag, Pt, Pd, Ni, and Fe films. Our method yields pure nanoporous Au without any secondary metal impurities. The electro-oxidation of methanol is demonstrated with our nanoporous Au

films. Remarkably, the reactivity and electron microscopy indicates high surface energy sites that are structurally more robust than those found in dealloyed nanoporous Au.

Results

Dry synthesis of mesoporous metal-films

Our dry synthesis of NPMs is based on the plasma treatment of a dense layer of nanoparticles deposited on a sacrificial thin polymer film. The process is schematically depicted in Fig. 1a. First, a 1 μm thick PMMA film is formed on a flat substrate, such as silicon, by spin-coating (see methods). A dense layer of metal nanoparticles with a diameter of about 10 nm is then obtained by e-beam evaporation of the metal onto the dried PMMA film at an oblique angle, here 80° (see Supplementary Fig. 1). The deposited metal atoms (*e.g.* Au, Ag, Pt, Pd, Ni, Fe) form random clusters on the substrate, which give rise to shadowing under oblique angle growth. This growth results in a rough nanostructured thin-film formed by a dense layer of metallic nanoparticles on top of the PMMA film. The substrate is then treated in a simple laboratory plasma system. During the plasma treatment, the PMMA starts to be etched by plasma ions that penetrate through the gaps between the metal nanoparticles (Fig. 1b1). As a result, the PMMA layer becomes rough and shrinks, as schematically shown in Fig. 1b2. The metal nanoparticles remain compact on the shrinking PMMA islands, since the interfacial energy is small (Fig. 1b2). At the same time, the metal nanoparticles are also bombarded with high-energy ions, which renders them mobile and causes their coalescence,³¹ facilitating cluster migration at low temperature (Fig. 1b3).³² We presume that the thermal energy is not high enough to liquefy the nanoparticles and cause their fusion, but rather that the coalescence leads to polycrystalline structures with many grain boundaries (see transmission electron microscope analysis below).^{33,34} When the remaining PMMA layer has been completely etched away, the porous metal structures will contact the substrate, where the metal is less mobile, since the interfacial energy is lower compared to that between nanoparticles and PMMA. Coalescence then ceases and the NPM remains robust despite further plasma treatment (Fig. 1b4, Supplementary Fig. 2).

-----FIGURE 1-----

Heating the nanoparticle-decorated PMMA film without plasma treatment did not yield nanoporous metallic structures (Supplementary Fig. 3). Hence, the process is not simply described by thermal effects. Rather, the etching of the PMMA plays an important role, in combination with surface tension effects and the aforementioned differences in interfacial energies between the metal and the two substrates. Fig. 1c shows scanning electron microscope (SEM) images of the resulting mesh-like NPMs fabricated with Au, Pt, Pd, and Ag, and the non-noble metals Ni and Fe. The films have pore sizes between 20 nm and hundreds of nanometers, and the ligament sizes of the metal filaments range from 10 nm to 80 nm. An exemplary

filament in the network is marked by red lines in Fig. 1c. The ligament or pore sizes can be tuned by controlling the conditions during the plasma treatment. For example, the nanoporous Au film (NPGF) can have a ligament sizes from 10 to 30 nm depending on the plasma time (Supplementary Fig. 4a-c). The nanoporous Au and Ni morphology can be controlled by means of the gas composition and the plasma power (Supplementary Fig. 4d-g). The kinetic energy of the ions in the plasma will vary according to the plasma conditions, resulting in different metal atom mobilities and different etching rates of the sacrificial PMMA layer.

We checked that the nanoporous networks are fully connected over larger areas by analyzing their conductivity. Depending on the film morphology, the sheet resistance of the Au-mesh film was in the range of 150 ~ 300 Ω/sq (4 probe measurement with a separation of ~1.3 mm between probes).

Purity of NPGF

Combustion analysis has been carried out to check for carbon residues in the NPGF. In this method, CO_2 resulting from the combustion of carbon present in the sample can be detected by infrared absorption.³⁵ Only 5 ppm (wt.) carbon residues from the plasma treatment could be detected. Hence, our NPMs do not contain any significant carbon residues from the plasma treatment. This is also confirmed in the subsequent X-ray photoelectron spectroscopy (XPS) and electrochemical analysis. As a note, the solubility of C in solid Au is known to reach only 50 ppm at temperatures above 1000 °C.

----- FIGURE 2 -----

We also carried out XPS measurements to evaluate the surface of the NPGF and its purity. The Au 4f signals from an NPGF on a Si wafer are plotted in Fig. 2a. The signals indicate a typical metallic Au 4f_{7/2} binding energy of 84.4 eV with the Au 4f_{5/2} component separated by a spin-orbit splitting of 3.7 eV.³⁶ The Au 4f_{7/2} component at 84.1 eV is known as the surface component of Au,³⁷ and is consistent with the large surface area of the NPGF. No peaks are seen that correspond to Au_2O_3 .³⁸ The O 1s and C 1s spectrum from the NPGF and a spin-coated PMMA layer are compared in Fig. 2b and 2c, respectively. The O 1s spectrum only shows one symmetric peak with a maximum at 533.5 eV which corresponds to SiO_2 of the Si substrate.³⁶ It is known that the O 1s peak for the metal oxide (excluding SiO_2) appears below 531 eV, and it is clearly absent in our NPGF. The typical O 1s spectrum from a film containing only spin-coated PMMA³⁹ disappears in the NPGF sample, indicating that PMMA is not present in the NPGF. The C 1s spectrum of PMMA in Fig. 2c shows multiple peaks at around 288.9, 286.9, 285.5, and 283.5 eV that originate from $\text{O}-\underline{\text{C}}=\text{O}$, $\underline{\text{C}}-\text{O}$, $\text{C}-\underline{\text{C}}=\text{O}$, and $-\underline{\text{C}}\text{H}_3$ binding states, respectively.³⁹ However, these peaks do

not appear in the NPGF sample (besides a very low intensity peak, which may relate to \underline{C} -O state), which corroborates that the PMMA is completely removed by the plasma. The overall C content is drastically reduced in the NPGF sample and originates from unavoidable contamination during sample transfer. Our combustion analysis and XPS results indicate that the PMMA is completely etched away and that no significant C impurities from PMMA remain after the plasma etching step. Compared to nanoporous Au prepared by dealloying or solution phase synthesis, the dry synthesis reported here is a much more convenient and general route to obtain NPM films that are also free from impurities.

TEM characterization of NPGF

Transmission electron microscopy (TEM) measurements were performed on the NPGF. Fig. 3a shows that the diameter and length of the ligaments in the NPGF range from 10 to 20 nm, and from 10 to 30 nm, respectively, and are relatively small compared to other reported nanoporous Au structures. Numerous pores are observed and the surface shows a high curvature including many concave and protruded structures, as well as many grain boundaries that are found on each curved region. One of the protruded sections in the image was also investigated by energy dispersive X-ray (EDX) mapping, as shown in Fig. 3b. The image shows that the Au is uniformly distributed over the NPGF structure. Moreover, C and O maps are uniform and indistinguishable from the background signals, in agreement with our previous observation that the NPGF do not contain any significant carbon or oxygen contamination from the sacrificial PMMA.

----- FIGURE 3 -----

High-resolution TEM (HR TEM) images revealing the atomic structure and crystallographic surface facets are shown in Fig. 3c. Fast Fourier transformation (FFT) images were also obtained in the regions of (i) ~ (iv) as depicted in Fig. 3c, clearly showing the polycrystallinity of the NPGF. The grains have a size of a few nanometers that is comparable to the initial size of metal nanoparticles. The measured lattice spacing in each region is 0.91, 2.35, 1.44, and 2.35 Å, which, respectively, correspond to the crystallographic orientations (420), (111), (220), and (111). This implies that our NPGF has various surface symmetries with multiple directions on the curved ligaments, even if the actual surface facets cannot be determined due to the projection effect in TEM. The polycrystalline nature of our NPGF is also confirmed by X-ray diffraction (XRD) measurements, as shown in Supplementary Fig. 5. The NPGF clearly shows an Au polycrystalline structures, with higher peak intensities than the as-deposited Au nanoparticles before plasma treatment indicating higher crystallinity of the NPGF. For the Au nanoparticles before plasma treatment an Au_2O_3 (311) peak also appears, which is not present after plasma treatment. This change is attributed to restructuring by bombardment with high-energy ions that removes the native oxide.

One can also clearly identify many grain boundaries between the nanograins. The retention of grain boundaries is explained by the higher energy required for the diffusion of metal atoms across the grain boundary compared to diffusion along a crystal facet.³⁴ The observed high density of grain boundary is a special feature of this type of nanoporous metals and explains the structural robustness of our NPGF. Most curved areas have various surface structures as investigated in other parts of the mesh structure (Supplementary Fig. 6). Multiple surface directions and many grain boundaries that have high surface energies and potentially high-indexed surfaces are ideal sites for catalytic reactions, as we shall confirm next.

Electrochemical properties of NPGF

To explore the catalytic properties of the NPMs we chose to investigate the catalytic properties of the NPGF using electrochemical measurements. Cyclic voltammograms (CVs) were recorded with nanoporous Au powder recovered from nanoporous gold films (NPGF powder) in acidic and in alkaline solutions. Figure 4a shows the CV of NPGF powder in 0.1 M H₂SO₄ at a scan rate of 10 mV s⁻¹. For these measurements, cavity microelectrodes were filled with NPGF powder. In the positively going scan, surface oxidation takes place from 1.2 V showing a very broad anodic peak with a maximum at 1.47 V. The broad peak is attributed to the rough and disordered Au surfaces.⁴⁰ A symmetric peak centered near 1.15 V is observed in the negatively going scan, which is associated with the reduction of the Au oxides formed during the preceding positively going scan. It is notable that our NPGF powder does not undergo significant surface reconstruction (10 cycles in 0.1 M H₂SO₄ are shown in the inset of Fig. 4a). This is in contrast to the behaviour of dealloyed nanoporous Au, which gives rise to surface restructuring and CVs that change significantly during the first potential cycles in 0.1 M H₂SO₄.⁴¹ A dealloyed nanoporous Au sample, measured in acidic solution already shows markedly different CVs after the second or third cycle, which is thought to arise from the removal of Ag impurities that relax the high energy low-coordinated atomic sites on the surface.⁴¹ Our NPGF powder, however, shows very stable CVs after the first cycle, implying that it has stable energetic atomic sites on the surface. The 10th cycle of CV in 0.1 M KOH solution (Fig. 4b) demonstrates that surface oxidation and reduction take place in the range of 0.6 V ~ 1.6 V. The pre-oxidation peak at potentials below 1.2 V has also been observed in conventional Au, and is related to the chemisorption of OH⁻ anions onto the Au surface. The main peaks during the positively going scan appear at 1.25, 1.4, and 1.5 V while the peaks forming during the negatively going scan appear at 1.09 V, which agrees very well with previously reported measurements on polycrystalline Au.⁴⁰ Significant surface reconstruction of NPGF powder occurs during the first two cycles, and afterwards the CVs remain stable (inset of Fig. 4b). As explained by the TEM images, this is attributed to the high density of grain boundaries,

which increase the energy barrier for metal atom diffusion compared to the surface diffusion in a dealloyed NPM structure. Our nanoporous gold films are particularly promising for (electro)catalysis, as they possess many grain boundaries and multiple surface directions that are nevertheless structurally robust.

----- FIGURE 4 -----

Under potential deposition (UPD) of lead (Pb) was carried out to examine the change of surface structures of a NPGF powder “as-prepared” (Fig. 4c), “pre-cycled in acid” solution (Fig. 4d), and “pre-cycled in alkaline” solution (Fig. 4e). The CV clearly shows well resolved UPD signals. Two intense peaks in the negatively going scan appear at 0.35 to 0.40V and 0.47 to 0.52 V and correspond to the Pb UPD on Au {111} and {110} domains, respectively. Two intense peaks in the positive going scan correspond to the anodic peaks at 0.45 to 0.50 V and 0.60 to 0.65 V attributed to oxidation of the Pb UPD layer. There is an additional peak between 0.35 to 0.40 V that has been reported to originate from defects near {111} domains. Note, that all peaks are very broad compared to the results from a single crystal Au electrode,⁴² indicating that each domain is most likely surrounded by defects. This result illustrates that the NPGF contains many low-coordinated atoms, such as steps and kinks. There is no significant change in the peak current and potential even after cycling in an acidic solution, which is a remarkable difference to the reported UPD results of dealloyed nanoporous Au.⁴³ This observation demonstrates again that the surface structure with high surface energy in the nanoporous gold films are more robust than for dealloyed nanoporous Au even under operating condition,⁴³ making the new material ideal for (electro)catalysis.

----- FIGURE 5 -----

The electrocatalytic performance of the NPGF powder was confirmed by investigation of electrochemical methanol oxidation. Figure 5a shows the CV of the NPGF powder in 0.1 M KOH with and without 1 M methanol. The NPGF powder was pre-cycled in KOH solution before methanol oxidation. Single crystal Au (111) is a less active catalyst for methanol oxidation especially in an acidic solution. However, Au with nanoscale roughness shows a higher activity due to the presence of low-coordinated atoms and surface defects.^{42,44-46} Our NPGF powder clearly facilitates strong methanol oxidation. Especially, the shape of the CV curve during methanol oxidation is very similar to that of dealloyed nanoporous Au *after* it has been pre-cycled in acid (to dissolve Ag impurities).⁴¹ This means that our NPGF is pure and exhibits a high surface area with many nanoscale pores and ligaments containing ideal surface structures for catalytic reactions. HR TEM was measured for the sample after methanol oxidation. As can be seen in Fig. 5b, the NPGF powder still has many facets in the curved region, meaning that the structure is very robust during the oxidation process, but remains highly catalytically active.

Discussion

Plasma-based dry synthesis is a facile and general method to produce nanoporous metals (NPMs). Since this approach does not include any wet-chemical reaction steps, it can be applied to a large number of metals including Au, Ag, Pt, Pd, Ni, and Fe. Considering that physical vapor deposition is used in the process, any metals that can be evaporated can be used in our scheme to form NPMs. This opens up the opportunity to employ co-deposition and hence extend the fabrication to nanoporous alloyed metal films. The plasma condition can be adjusted to the nature of the metal film. Non-noble metal films were obtained using a mixture of Ar and H₂ to prevent the oxidation of the metal during removal of the PMMA film.

The NPM structures are shown to be highly porous with highly curved nanoscale bicontinuous ligaments. The nanoporous gold films were examined with high resolution TEM and found to possess many low-coordinated atomic sites. The films are free from impurities and highly reactive. Especially compared with conventional dealloyed nanoporous gold, our films are very stable, as revealed by potential cycling in acids and bases and Pb underpotential deposition.

The method described herein yields ultra-thin NPM structures, that can be tuned in material composition and pore structure and thus suggest further promising applications as transparent conducting electrodes (see Supplementary Fig. 7, Supplementary Table 1). It is also possible to lift off the films from the substrate and realize free-standing NPM films (Supplementary Fig. 8). We expect that our dry synthesis method, which is robust and which can reproducibly produce impurity-free films, will open up new opportunities in the application of nanoporous metallic films.

Methods

Fabrication of NPMs

Poly(methyl methacrylate) (PMMA, average Mw ~ 120,000, from Sigma Aldrich) was dissolved (1.5 wt. %) in chloroform for 12 h at room temperature using magnetic stirring. The solution was spin-coated on a Si wafer substrate (Boron doped, <100> orientation, native oxide covered), cleaned in Piranha solution (a mixture of 3 parts of concentrated H₂SO₄ and 1 part of 30% H₂O₂ for 30 min) at 1000 rpm for 1 min. Each metal (> 99.99 % purity) was evaporated by e-beam on a PMMA thin film at room temperature with an oblique angle of 80 °, with a rate of 0.05 nm/s, 10 nm target thickness considering tooling factor, and rotation speed 0.72 ° / sec. The deposited Au film was plasma-treated in 0.4 mbar air ambient with 200 W for 15 min. The Ag NPM film was obtained after treatment 0.4 mbar Ar ambient with 200 W for 15 min, and other NPM films (Pt, Pd, Ni, Fe) in 0.4 mbar W10 ambient (Ar 90 %, H₂ 10 %) with 300 W for 15 min.

Purity analysis

The nanoporous gold film was fabricated on a Si substrate. After complete etching of PMMA, the film was used for combustion analysis and XPS. A PMMA film coated on Si substrate without a metal layer was also characterized, for reference.

For the combustion analysis a sample was burned in a flowing stream of oxygen.³⁵ Very low concentrations of carbon can be detected (resolution down to 1 ppm (wt.)). We compared the absorption spectra of three NPGFs on Si substrates and three cleaned bare Si substrates. Any CO₂ was detected by absorption of infrared radiation. The measurement was repeated three times.

XPS measurements were performed on a Theta Probe Angle-Resolved X-ray Photoelectron Spectrometer System (Thermo Fisher Scientific Inc.). The base pressure was 3×10^{-10} mbar and the excitation X-ray source was a monochromatic Al K α radiation (100W, $h\nu$ was 1486.68 eV). Survey spectra were measured at a pass energy of 200 eV, followed by high-resolution spectra for Au 4f, C 1s, O 1s, and Si 2p with a pass energy of 10 eV, a step size of 0.05 eV and a dwell time of 100 ms. Charge was corrected for all the binding energies by shifting the C-C (or C-H) part of the C 1s peak to 284.8 eV. Peak fitting was performed using the Avantage software (version 5.9904).

Characterization of electrochemical properties

To remove the NPGF off the substrate, a thicker PMMA film (5 wt. % spin-coated at 1000 rpm for 1 min) was used. After plasma treatment, the PMMA film was not entirely removed and was thus able to support the NPGF. This sample was immersed in pure acetone to dissolve the PMMA film to obtain a free-standing NPGF that could be lifted-off. NPGF was collected in the Teflon Petri dish and dried for 3 h in Ar at ambient conditions. The chunks of the film obtained by this method were the starting material to be loaded into cavity microelectrodes for the electrochemical experiments.

Cavity microelectrodes (CME) were produced by sealing a 1.5 cm Au wire of 100 μ m diameter (99.99+%, Goodfellow, Friedberg, Germany) in a borosilicate glass capillary which was previously heated to form a tip. The assembly was ground with grade 1500 abrasive paper to expose the disk-shape cross-section of the Au wire followed by polishing with abrasive papers of 15, 9, 3, and 1 μ m grain size. Subsequently, the disk-shape cross section is polished to mirror finish using a microgrinder (EG-401, Narishige, Tokyo, Japan).

Finally, the Au wire inside the capillary was connected to a Cu wire with silver-epoxy glue (EPO-TEKS, John P. Kummer GmbH, Germany).

The cavities were formed by potentiostatic dissolution of the exposed Au at +1.1 V vs. a saturated calomel electrode (SCE, from ALS, Tokyo, Japan) in 1 M HCl during 60 s and afterwards cycled 5 times at 100 mV s⁻¹ between 0.5 V and 1.5 V vs. SCE. The quality of the polish on the microelectrodes and the depth of the cavities [(21 ± 1) μm] was verified using a confocal laser scanning microscope (TCS SP2, Leica Microsystems GmbH, Germany) with a HC PL Fluotar 50×/0.8 dry lens. The cavity is cleaned by immersion in Piranha solution for 1 h and transferred to ultrapure water for at least 24 h. The cavity was filled by slightly pressing the CME into the NPGF powder that has been lifted off (as described overleaf). The end of the filled CME was washed with ultrapure water and any excess NPGF outside the cavity was wiped off with a soft cloth. The filling is monitored by inspection with a 6× magnifying lens.

The electrochemical cell is built with a 25 mL glass vial and a Teflon cap with five necks. A CME filled with the sample was used as the working electrode, and an Au coil as the auxiliary electrode. The reference electrodes were Hg/HgSO₄/K₂SO₄(Sat) (from ALS, Japan) in Cl⁻-free acid media and a Hg/HgO/1 M NaOH (from ALS, Japan) in alkaline media. Electrochemical characterization was performed on a PGSTAT128N potentiostat with an analog scan generator (Autolab-Metrohm, Filderstadt, Germany with scan250 and NOVA 2.1 software).

All glassware was cleaned by immersion in 1 g/L KMnO₄ solution acidified with 20 mL/L 96 % H₂SO₄ for at least 24 h. To remove the excess of MnO₄⁻, the glassware was immersed in 40 mL/L 30 % H₂O₂ solution acidified with 20 mL/L of 96 % H₂SO₄, until no visual evidence of purple color was detected. Finally, it was rinsed with ultrapure water and boiled three times.

For the UPD experiments, an alkaline Pb-containing solution was prepared by dissolving the weighted amount of KOH in half of the final volume, followed by addition of Pb(NO₃)₂ and finally filling up water to the final volume. This order is important to avoid the oxidation of Pb²⁺ to Pb⁴⁺ promoted by the dissolved oxygen in strongly alkaline medium.

All potentials are reported versus the reversible hydrogen electrode (RHE) by using the equation $E_{\text{RHE}} = E_{\text{SHE}} + 0.140 \text{ V} + (0.059 \cdot \text{pH})$, where the potential against the standard hydrogen electrodes is obtained by constant potential distance to the used laboratory reference electrodes $E_{\text{SHE}} = E_{\text{Hg|HgO|1 M NaOH}} + 0.14 \text{ V}$ or $E_{\text{SHE}} = E_{\text{Hg|HgSO}_4|\text{K}_2\text{SO}_4(\text{sat})} + 0.64 \text{ V}$.

Electron microscopy

For SEM, a NPGF was used that has been fabricated by the method described herein on a Si substrate after complete etching of PMMA. For the TEM preparation of the “as-prepared” NPGF, the same method was used as for the preparation before the electrochemical measurement. The PMMA film was not etched entirely, and the sample was immersed in pure acetone to dissolve the PMMA film to obtain a free-standing Au film that could be lifted-off. The film was then picked up with a plasma-cleaned TEM carbon grid, followed by drying in Ar flow for an hour. For TEM-EDS measurement, a SiO₂ grid was used to avoid strong carbon signals from the grid.

For HR TEM of the NPGF after methanol oxidation, the Au-film filled microelectrode was sonicated in pure ethanol (50 µL) for 3 min in an Eppendorf tube. Then 5 µL of solution was drop-casted on a plasma-cleaned TEM carbon grid, and dried in Ar flow for 5 min. Solution casting and drying was repeated 10 times.

A 200 kV JEOL ARM200CF scanning transmission electron microscope equipped with a cold field emission electron source, and a CETCOR image corrector (CEOS GmbH) was used to obtain HR TEM images, and the ZEISS SESAM (sub-electronvolt-sub-angstrom-microscope) with a field emission gun (200 kV), equipped with a monochromator, MANDOLINE-filter and a 60 mm² Thermo Fischer ultradry EDX detector was used to obtain the TEM EDS data.

Data availability

The authors declare that all experimental data supporting this study are included in the published article and its Supplementary Information. The raw data are also available from the authors upon reasonable request.

References

1. Tappan, B. C., Steiner III, S. A. & Luther, E. P. Nanoporous metal foams. *Angew. Chem. Int. Ed.* **49**, 4544–4565 (2010).
2. Koya, A. N., Zhu, X., Ohannesian, N., Yanik, A. A., Zaccaria, R. P., Krahne, R., Shih, W.-C. & Garoli, D. Nanoporous metals: from plasmonic properties to applications in enhanced spectroscopy and photocatalysis. *ACS Nano* **15**, 6038–6060 (2021)
3. Zhang, R. & Olin, H. Porous gold films—a short review on recent progress. *Materials* **7**, 3834–3854 (2014).

4. Jin, T., Terada, M., Bao, M. & Yamamoto, Y. Catalytic performance of nanoporous metal skeleton catalysts for molecular transformations. *ChemSusChem* **12**, 2936–2954 (2019).
5. Khristosov, M. K., Dishon, S., Noi, I., Katsman, A. & Pokroy, B. Pore and ligament size control, thermal stability and mechanical properties of nanoporous single crystals of gold. *Nanoscale* **9**, 14458–14466 (2017).
6. Fujita, T., Guan, P., McKenna, K., Lang, X., Hirata, A., Zhang, L., Tokunaga, T., Arai, S., Yamamoto, Y., Tanaka, N., Ishikawa, Y., Asao, N., Yamamoto, Y., Erlebacher, J. & Chen, M. Atomic origins of the high catalytic activity of nanoporous gold. *Nat. Mater.* **11**, 775–780 (2012).
7. Fajín, J. L. C., Cordeiro, M. N. D. S. & Gomes, J. R. B. On the theoretical understanding of the unexpected O₂ activation by nanoporous gold. *Chem. Commun.* **47**, 8403–8405 (2011).
8. Wang, H., Fang, Q., Gu, W., Du, D., Lin, Y. & Zhu, C. Noble metal aerogels. *ACS Appl. Mater. Interfaces* **12**, 52234–52250 (2020).
9. Hiekel, K., Jungblut, S., Georgi, M. & Eychmüller, A. Tailoring the morphology and fractal dimension of 2D mesh-like gold gels. *Angew. Chem. Int. Ed.* **132**, 12146–12152 (2020).
10. Welch, A. J., DuChene, J. S., Tagliabue, G., Davoyan, A., Cheng, W.-H. & Atwater, H. A. Nanoporous gold as a highly selective and active carbon dioxide reduction catalyst. *ACS Appl. Energy Mater.* **2**, 164–170 (2019).
11. Chen, Q., Ding, Y. & Chen, M. Nanoporous metal by dealloying for electrochemical energy conversion and storage. *MRS Bull.* **43**, 43–48 (2018).
12. Qiu, H.-J., Li, X., Xu, H.-T., Zhang, H.-J. & Wang, Y. Nanoporous metal as a platform for electrochemical and optical sensing. *J. Mater. Chem. C* **2**, 9788–9799 (2014).
13. Vidal, C., Wang, D., Schaaf, P., Hrelescu, C. & Klar, T. A. Optical plasmons of individual gold nanosponges. *ACS Photonics* **2**, 1436–1442 (2015).
14. Erlebacher, J., Aziz, M. J., Karma, A., Dimitrov, N. & Sieradzki, K. Evolution of nanoporosity in dealloying. *Nature* **410**, 450–453 (2001).
15. Pedireddy, S., Lee, H. K., Tjiu, W. W., Phang, I. Y., Tan, H. R., Chua, S. Q., Troadec, C. & Ling, X. Y. One-step synthesis of zero-dimensional hollow nanoporous gold nanoparticles with enhanced methanol electrooxidation performance. *Nat. Commun.* **5**, 4947 (2014).

16. Khristosov, M. K., Bloch, L., Burghammer, M., Kauffmann, Y., Katsman, A. & Pokroy, B. Sponge-like nanoporous single crystals of gold. *Nat. Commun.* **6**, 8841 (2015).
17. Lee, D. H., Park J. S., Hwang J. H., Kang, D. H., Yim, S.-Y. & Kim, J. H. Fabrication of hollow nanoporous gold nanoshells with high structural tunability based on the plasma etching of polymer colloid templates. *J. Mater. Chem. C* **6**, 6194-6199 (2018).
18. Rebbecchi, T. A. & Chen, Y. Template-based fabrication of nanoporous metals. *J. Mater. Res.* **33**, 2–15 (2018).
19. Haupt, M., Miller, S., Glass, R., Arnold, M., Sauer, R., Thonke, K., Möller, M. & Spatz, J. P. Nanoporous gold films created using templates formed from self-assembled structures of inorganic–block copolymer micelles. *Adv. Mater.* **15**, 829–831 (2003).
20. Bartlett, P. N., Baumberg, J. J., Birkin, P. R., Ghanem, M. A. & Netti, M. C. Highly ordered macroporous gold and platinum films formed by electrochemical deposition through templates assembled from submicron diameter monodisperse polystyrene spheres. *Chem. Mater.* **14**, 2199–2208 (2002).
21. Attard, G. S., Bartlett, P. N., Coleman, N. R. B., Elliott, J. M., Owen, J. R., & Wang, J. H. Mesoporous platinum films from lyotropic liquid crystalline phases. *Science* **278**, 838–840 (1997)
22. Qian, F., Troksa, A., Fears, T. M., Nielsen, M. H., Nelson, A. J., Baumann, T. F., Kucheyev, S. O., Han, T. Y.-J., & Bagge-Hansen, M. Gold aerogel monoliths with tunable ultralow densities. *Nano Lett.* **20**, 131–135 (2020).
23. Liu, P., Guan, P., Hirata, A., Zhang, L., Chen, L., Yuren, W., Ding, Y., Fujita, T., Erlebacher, J. & Chen, M. Visualizing under-coordinated surface atoms on 3D nanoporous gold catalysts. *Adv. Mater.* **28**, 1753–1759 (2016).
24. Guo, X., Zhang, C., Tian, Q. & Yu, D. Liquid metals dealloying as a general approach for the selective extraction of metals and the fabrication of nanoporous metals: a review. *Mater. Today Commun.* **26**, 102007 (2021).
25. McCue, I., Benn, E., Gaskey, B. & Erlebacher, J. Dealloying and dealloyed materials. *Annu. Rev. Mater. Res.* **46**, 263–286 (2016).
26. Graf, M., Haensch, M., Carstens, J., Wittstock, G. & Weissmüller, J. Electrocatalytic methanol oxidation with nanoporous gold: microstructure and selectivity. *Nanoscale* **9**, 17839–17848 (2017).

27. Lackmann, A., Bäumer, M., Wittstock, G. & Wittstock, A. Independent control over residual silver content of nanoporous gold by galvanodynamically controlled dealloying. *Nanoscale* **10**, 17166–17173 (2018).
28. Wittstock, A., Neumann, B., Schaefer, A., Dumbuya, K., Kübel, C., Biener, M. M., Zielasek, V., Steinrück, H.-P., Gottfried, J. M., Biener, J., Hamza, A. & Bäumer, M. Nanoporous Au: an unsupported pure gold catalyst? *J. Phys. Chem. C* **113**, 5593–5600 (2009).
29. Jin, Y., Li, R. & Zhang, T. Formation of nanoporous silver by dealloying Ca–Ag metallic glasses in water. *Intermetallics* **67**, 166–170 (2015).
30. Madern, N., Monnier, J., Cachet–Vivier, C., Zhang, J., Bastide, S., Paul–Boncour, V. & Latroche, M. Anisotropic nanoporous nickel obtained through the chemical dealloying of Y_2Ni_7 for the comprehension of anode surface chemistry of Ni–MH batteries. *ChemElectroChem* **6**, 5022–5031 (2019).
31. Pashley, D. W., Stowell, M. J., Jacobs, M. H. & Law, T. J. The growth and structure of gold and silver deposits formed by evaporation inside an electron microscope. *Philos. Mag. J. Theor. Exp. Appl. Phys.* **10**, 127–158 (1964).
32. Winkler, K., Wojciechowski, T., Liszewska, M., Górecka, E. & Fiałkowski, M. Morphological changes of gold nanoparticles due to adsorption onto silicon substrate and oxygen plasma treatment. *RSC Adv.* **4**, 12729–12736 (2014).
33. Hoffman, R. W. Stresses in thin films: the relevance of grain boundaries and impurities. *Thin Solid Films* **34**, 185–190 (1976).
34. Jeffers, G., Dubson, M. A. & Duxbury, P. M. Island-to-percolation transition during growth of metal films. *J. Appl. Phys.* **75**, 5016–5020 (1994).
35. López, G. A. & Mittemeijer, E. J. The solubility of C in solid Cu. *Scr. Mater.* **51**, 1–5 (2004).
36. Moulder, J. F. Handbook of X-ray photoelectron spectroscopy: a reference book of standard spectra for identification and interpretation of XPS data. Physical Electronics Division, Perkin-Elmer Corporation, (1992).
37. Passiu, C., Rossi, A., Weinert, M., Tysoe, W., & Spencer N. D. Probing the outermost layer of thin gold films by XPS and density functional theory. *Appl. Surf. Sci.* **507**, 145084 (2020).

38. Yamamoto, M., Matsumae, T., Kurashima, Y., Takagi, H., Suga, T., Itoh, T. & Higurashi, E. Comparison of argon and oxygen plasma treatments for ambient room-temperature wafer-scale Au–Au bonding using ultrathin Au films. *Micromachines* **10**, 119 (2019).
39. Piao, H., Fairley, N. & Walton, J. Application of XPS imaging analysis in understanding interfacial delamination and X-ray radiation degradation of PMMA. *Surf. Interface Anal.* **45**, 1742–1750 (2013).
40. Zhang, J., Liu, P., Ma, H. & Ding, Y. Nanostructured porous gold for methanol electro-oxidation. *J. Phys. Chem. C* **111**, 10382–10388 (2007).
41. Silva Olaya, A. R., Zandersons, B. & Wittstock, G. Restructuring of nanoporous gold surfaces during electrochemical cycling in acidic and alkaline media. *ChemElectroChem* **7**, 3670–3678 (2020).
42. Hernández, J., Solla-Gullón, J., Herrero, E., Aldaz, A. & Feliu, J. M. Methanol oxidation on gold nanoparticles in alkaline media: unusual electrocatalytic activity. *Electrochim. Acta* **52**, 1662–1669 (2006).
43. Silva Olaya, A. R., Zandersons, B. & Wittstock, G. Effect of the residual silver and adsorbed lead anions towards the electrocatalytic methanol oxidation on nanoporous gold in alkaline media. *Electrochim. Acta* **383**, 138348 (2021).
44. Rodriguez, P. & Koper, M. T. M. Electrocatalysis on gold. *Phys. Chem. Chem. Phys.* **16**, 13583–13594 (2014).
45. Borkowska, Z., Tymosiak-Zielinska, A. & Shul, G. Electrooxidation of methanol on polycrystalline and single crystal gold electrodes. *Electrochim. Acta* **49**, 1209–1220 (2004).
46. Borkowska, Z., Tymosiak-Zielinska, A. & Nowakowski, R. High catalytic activity of chemically activated gold electrodes towards electro-oxidation of methanol. *Electrochim. Acta* **49**, 2613–2621 (2004).

Competing interests

The authors declare no competing interests.

Figures

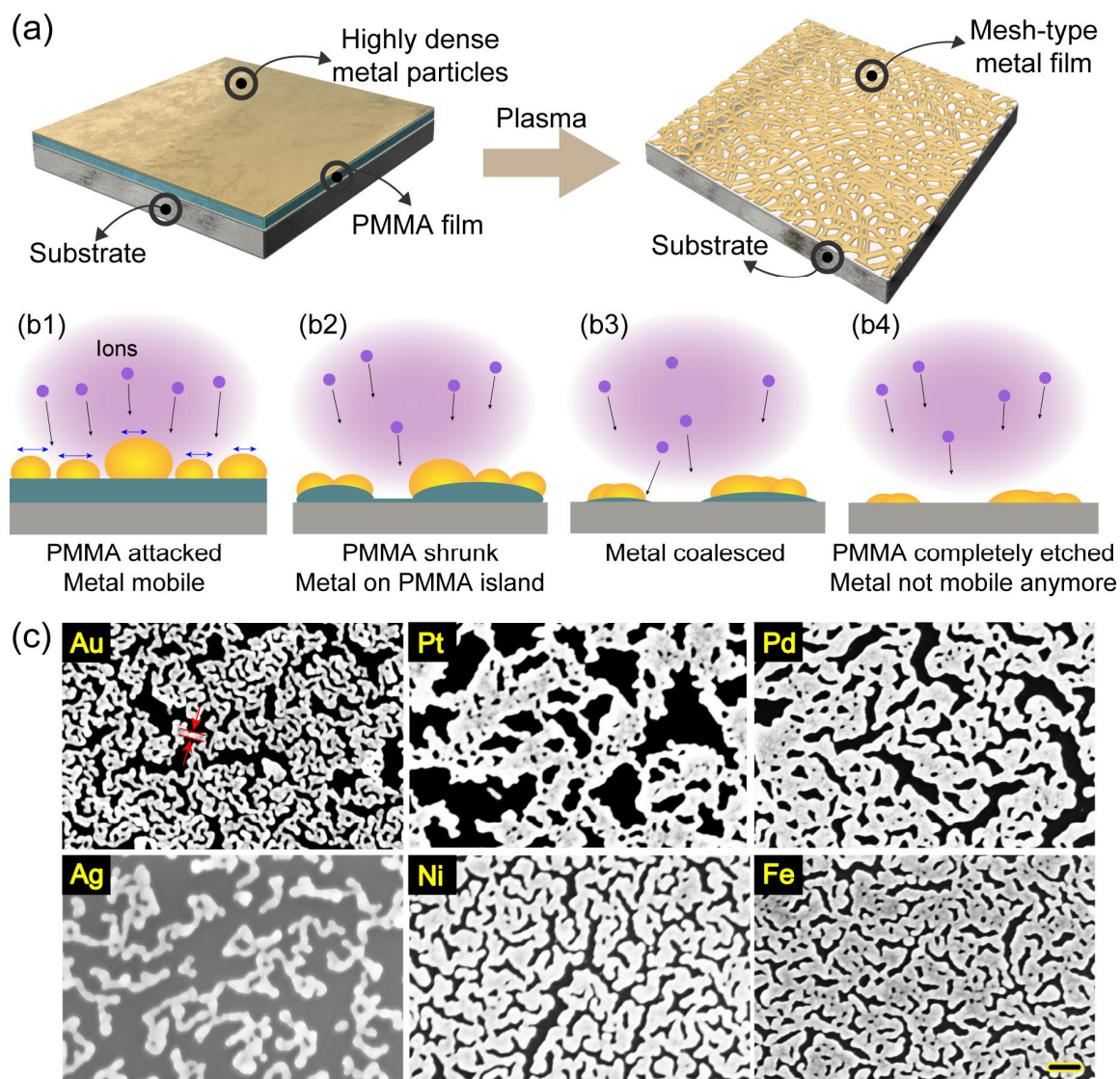


Figure 1. (a) Schematic: dry synthesis of nanoporous metals (NPMs). The deposited metal nanoparticles on the PMMA layer transform to NPM structures after plasma treatment. Cross-section schematics that show how the metal nanoparticles are thought to evolve over time (see text for details) are seen in (b1) to (b4). (c) SEM images of different NPMs. Scale bar 100 nm. Red lines with arrows indicate the filaments of the structure.

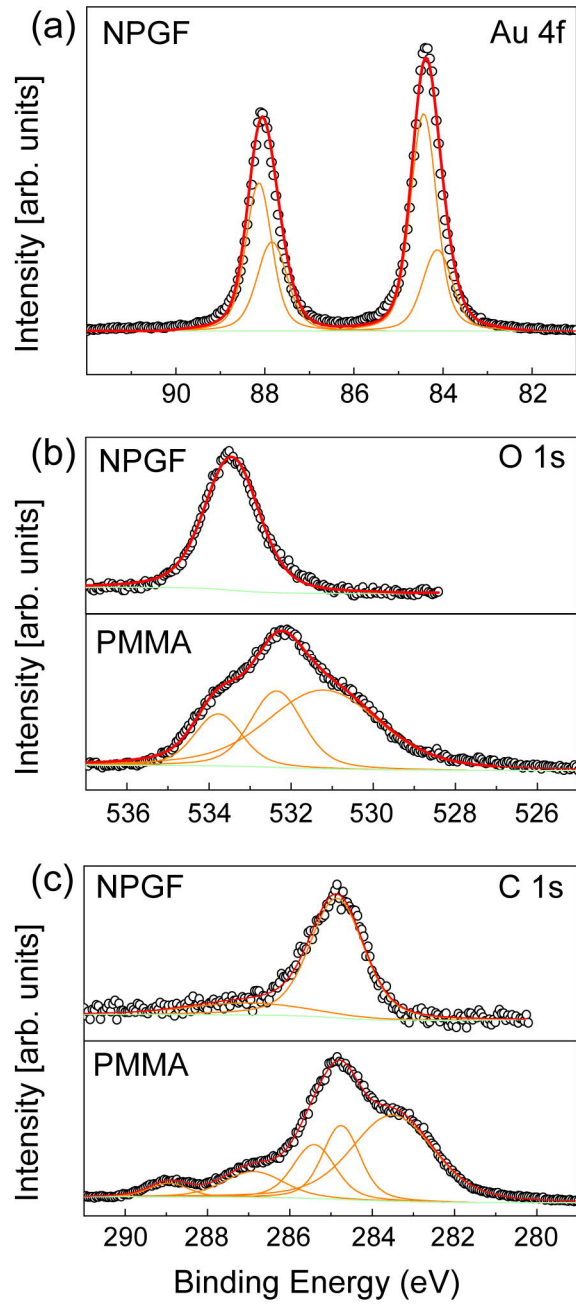


Figure 2. XPS results of NPGF sample. (a) Au 4f of NPGF sample. (b) Comparison of the O 1s spectrum and (c) C 1s spectrum from the NPGF sample and a spin-coated PMMA sample. Black dots are from the measurement and red lines are fitted curves.

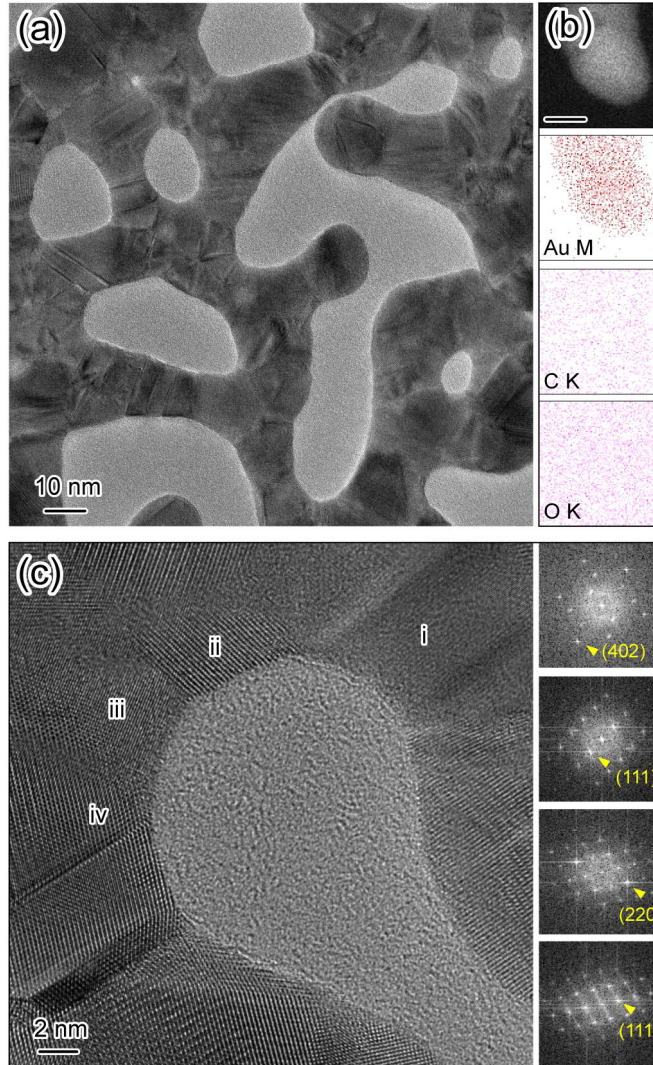


Figure 3. TEM measurements of NPGF. (a) Relatively low magnification image of NPGF showing highly curved ligaments and pores. Ligament sizes are 10 – 30 nm, which is relatively small compared to reported nanoporous Au structures made by dealloying. (b) TEM-EDX analysis of a specific protruded region of NPGF. Au M signal is clear, but C K and O K signals are not distinguishable from background signals. (c) Image of a concave region. FFT images were obtained from each region, and are shown in the right column in the order i to iv. The NPGF has surfaces with multiple directions especially in curved regions, and many grain boundaries between grains few nanometer in size.

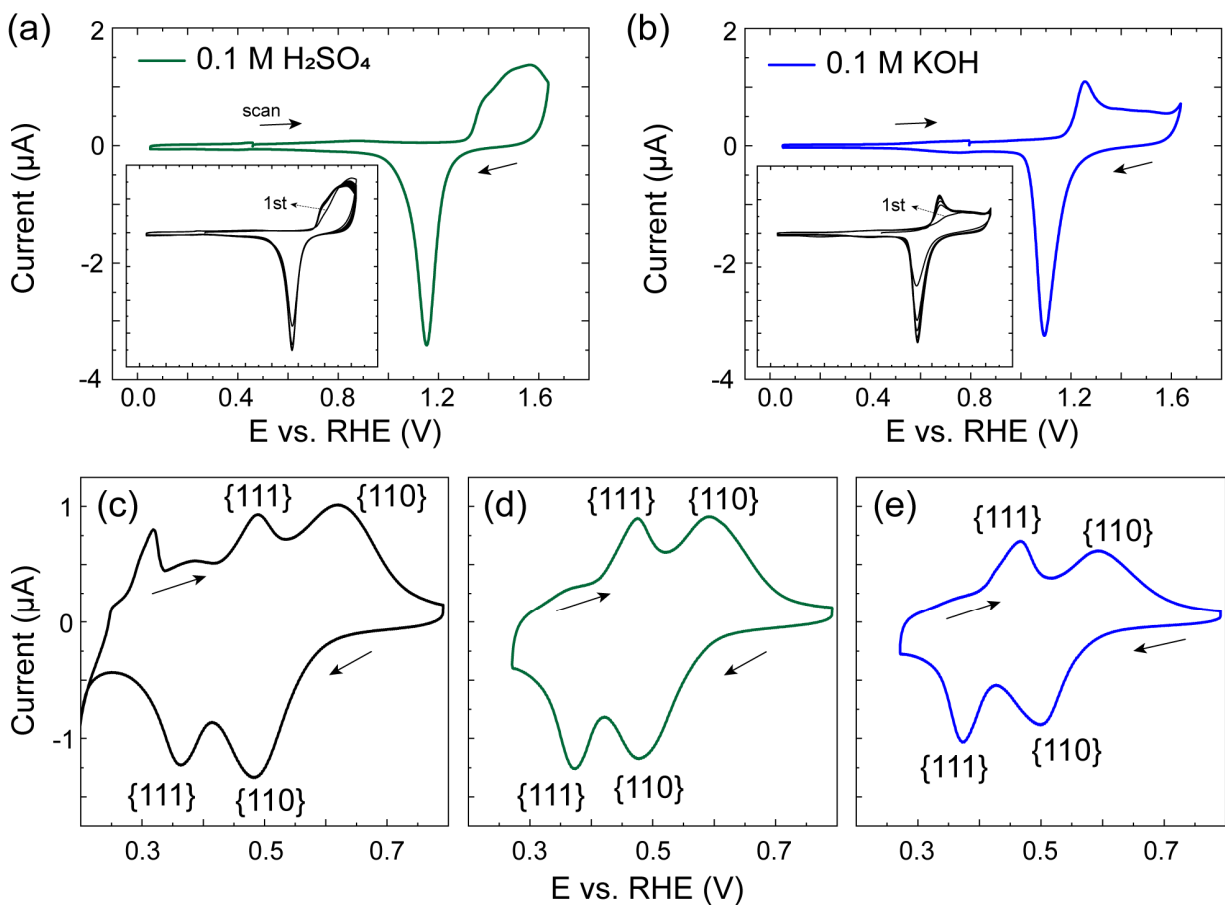


Figure 4. CVs of NPGF powder in (a) 0.1 M H₂SO₄ acidic and (b) 0.1 M KOH alkaline solutions. The main plot shows the the 10th cycle, the insets shows the cycles 1-10. UPD of Pb on NPGF powder (c) as-prepared, (d) on NPGF powder pre-cycled in acidic solution, and (e) on NPGF powder pre-cycled in alkaline solution. Major peaks during Pb under-potential deposition and dissolution correspond to processes at {111} and {110} domains. Broad peaks are indicative for many defects in NPGF powder. All CVs were measured at 10 mV s⁻¹.

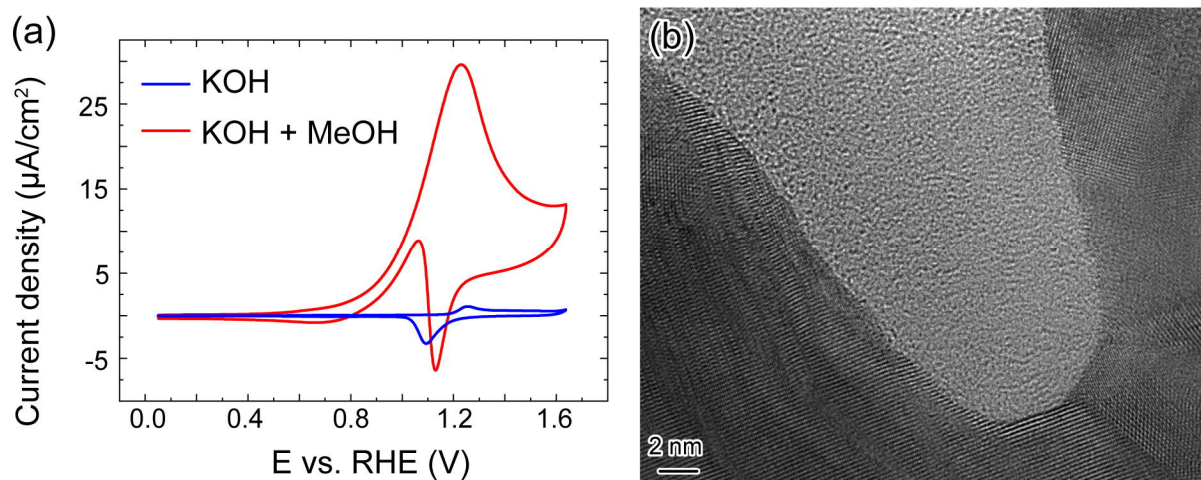


Figure 5. Electrooxidation of methanol at NPGF powder. (a) Comparison of CVs in 0.1 M KOH solution and in 0.1 M KOH + 1 M methanol solution. Scan rate is 10 mV s^{-1} . The red curve shows strong methanol oxidation attributed to the high surface area combined with many reactive surface structures important for catalytic reactions. (b) HR TEM image of the NPGF powder *after* methanol oxidation showing various grains and grain boundaries, and multiple surface directions, indicating the robustness of the NPGF under catalytic conditions.

Supplementary Information

Dry Synthesis of Nanoporous Metallic Films

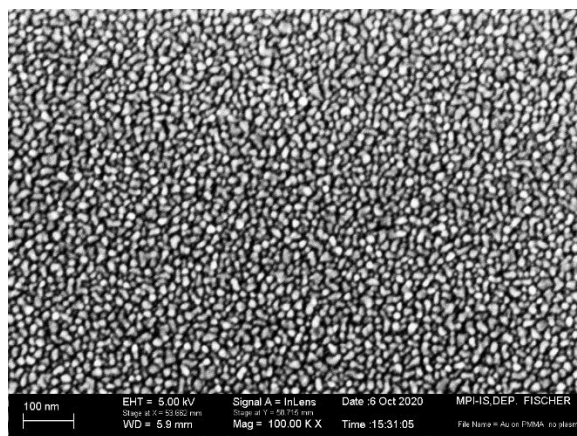
Hyunah Kwon ¹, Hannah-Noa Barad ¹, Alex Ricardo Silva Olaya ², Mariana Alarcon-Correa ¹, Kersten Hahn ³, Gunther Richter ¹, Gunther Wittstock ², Peer Fischer ^{1,4,*}

¹ Max Planck Institute for Intelligent Systems, Heisenbergstrasse 3, 70569 Stuttgart, Germany

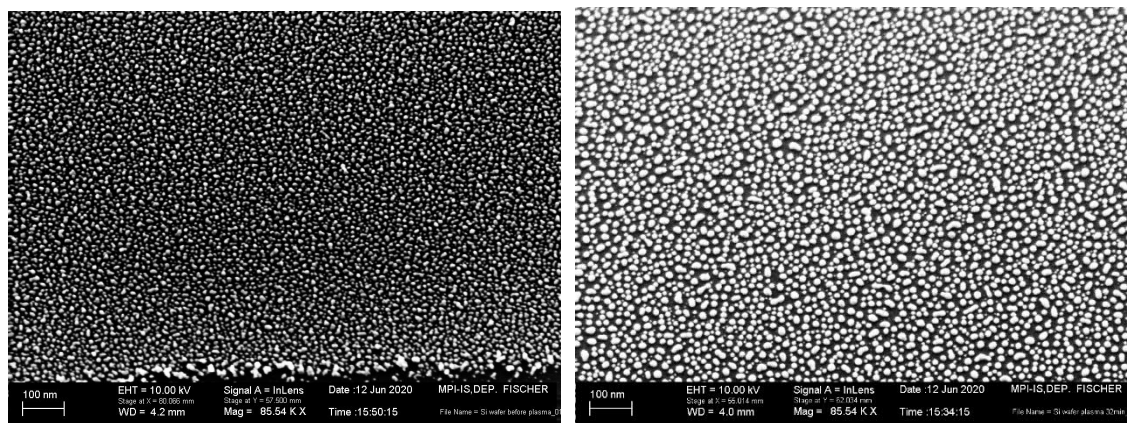
² School of Mathematics and Science, Department of Chemistry, Carl von Ossietzky University of Oldenburg, 26111 Oldenburg, Germany

³ Max Planck Institute for Solid State Research, Heisenbergstrasse 1, 70569 Stuttgart, Germany

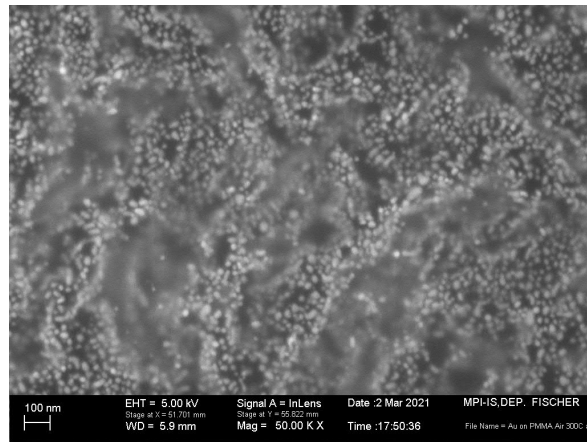
⁴ Institute of Physical Chemistry, University of Stuttgart, Pfaffenwaldring 55, 70569 Stuttgart, Germany



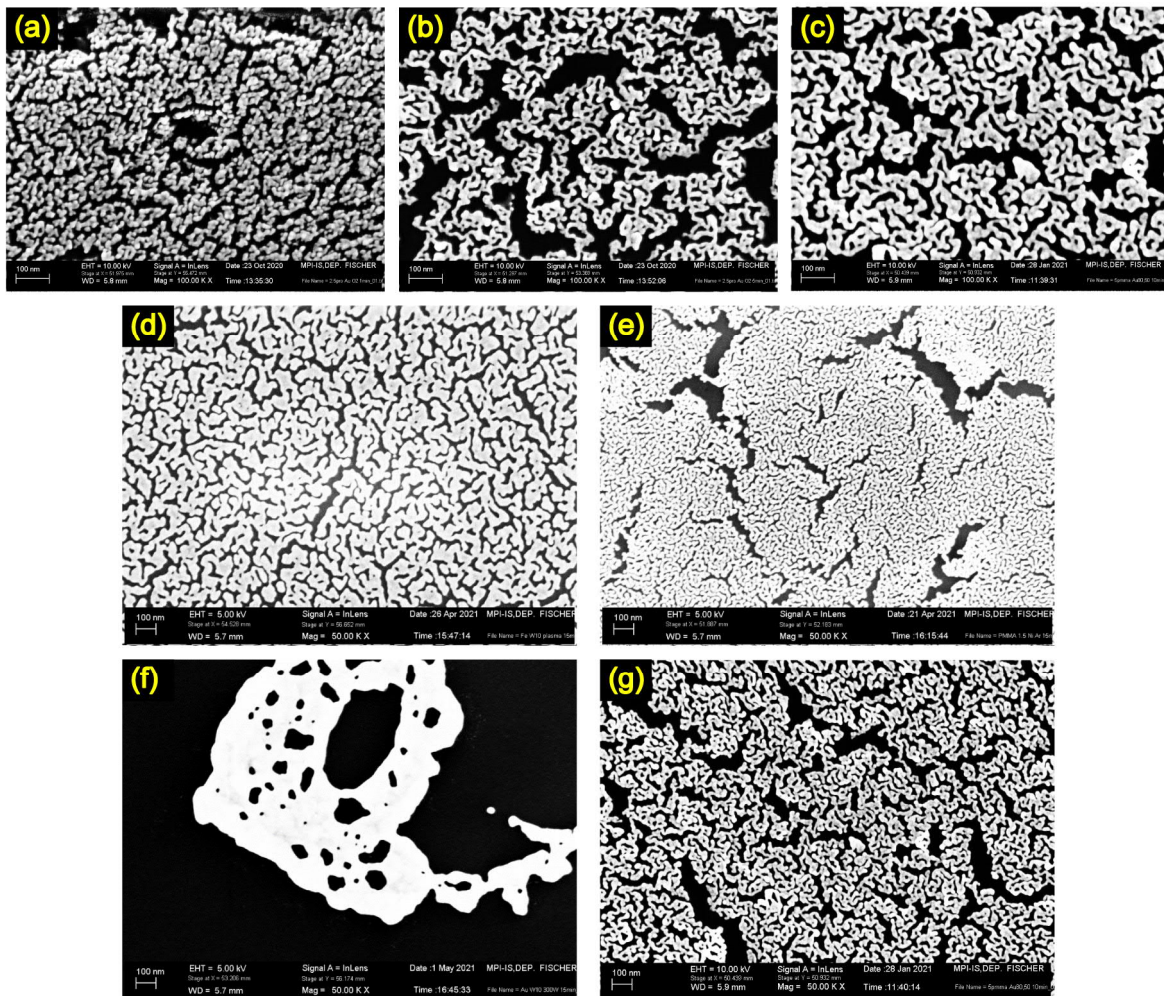
Supplementary Figure 1. Layer of Au nanoparticles on a PMMA substrate, deposited with oblique angle (or glancing angle deposition, GLAD) (50 nm, 80 deg).



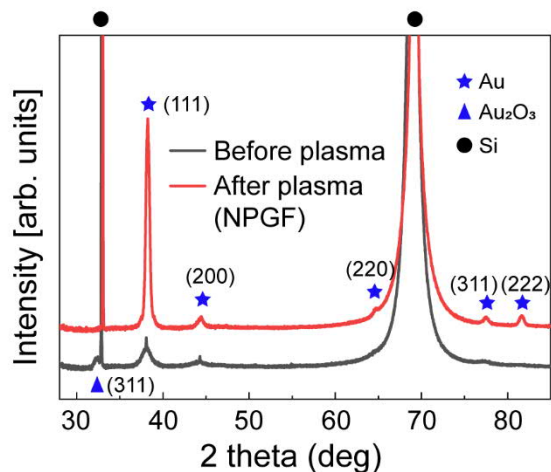
Supplementary Figure 2. Layer of Au nanoparticles on a Si wafer before (left) and after (right) plasma treatment. Several small (<10 nm) nanoparticles coalesce initially, but the resultant larger nanoparticles (larger than ~20 nm) are no longer mobile enough, and do not lead to networked structures on a Si wafer.



Supplementary Figure 3. Au nanoparticles on PMMA with heating at 300 °C for 5 min.

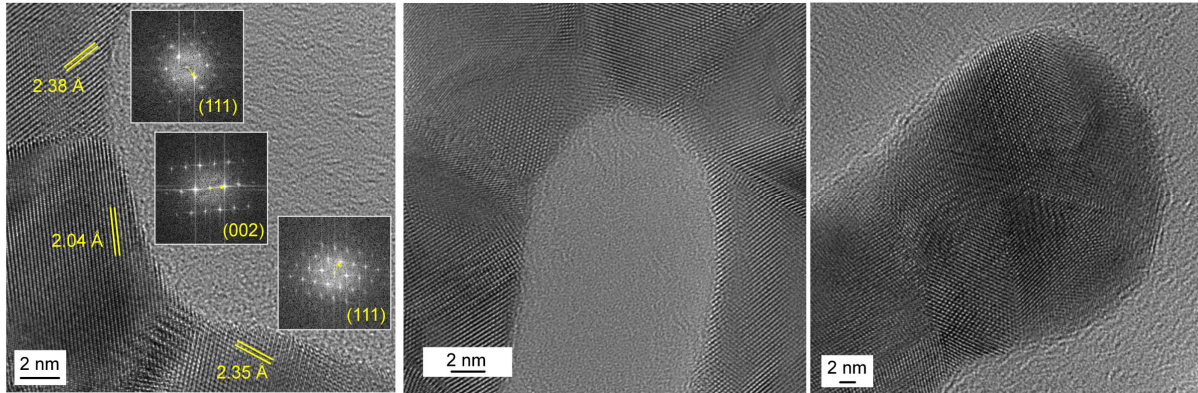


Supplementary Figure 4. Morphology control of NPM as a function of the plasma conditions. (a-c) NPGF with varying plasma treatment times (a) 1 min, (b) 5 min, and (c) 10 min, 0.4 mbar air ambient with 200 W. (d-e) Nanoporous Ni film for different plasma conditions: (d) 0.4 mbar W10 (Ar 90 %, H₂ 10 %) ambient with 300 W for 15 min, and (e) 0.4 mbar Ar ambient with 200 W for 15 min. (f-g) NPGF for different plasma conditions: (f) 0.4 mbar W10 (Ar 90 %, H₂ 10 %) ambient with 300 W for 15 min, and (g) 0.4 mbar air ambient with 200 W for 10 min.

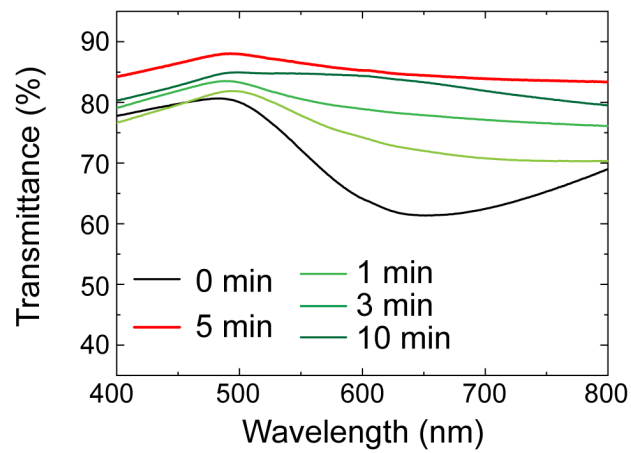


Supplementary Figure 5. X-ray diffraction (source: Cu K α radiation) of NPGF (red) and as-deposited Au on PMMA layer (black) samples. Scan rate is 7°/hour. Peaks from Au are much enhanced after plasma treatment. Si peaks are from forbidden (200) reflection¹ and (400). A peak near 32° from the as-deposited Au sample arises Au₂O₃, which is naturally formed during the deposition. This peak disappears in the NPGF sample.

1. Zaumseil, P. High-resolution characterization of the forbidden Si 200 and Si 222 reflections. *J. Appl. Cryst.* **48**, 528–532 (2015).



Supplementary Figure 6. HR TEM images of concave and protruded regions of a NPGF. Different grains with grain boundaries and a number of different surface facets are clearly seen.

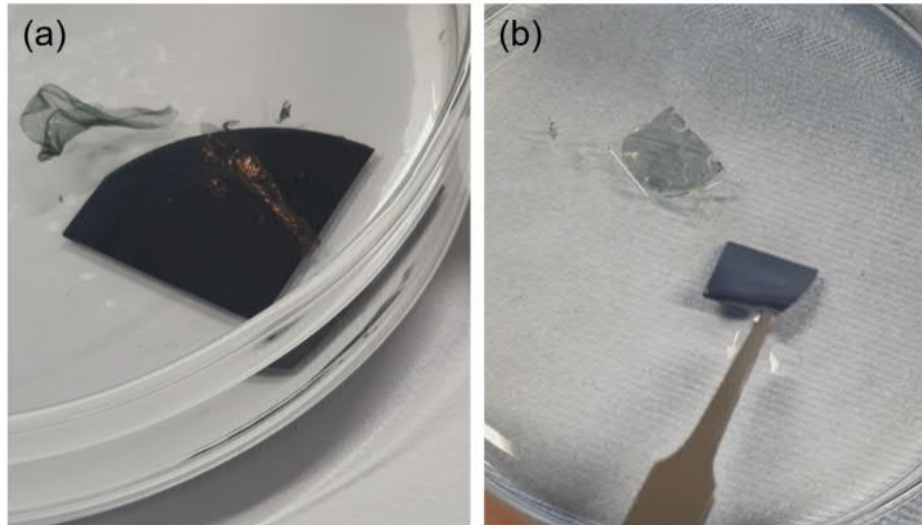


Supplementary Figure 7. Measured transmittance of NPGF depending on plasma time.

Supplementary Table 1. Measured sheet resistance of NPGF.

Sample preparation	Sheet resistance
No plasma	Not measurable
Air, 0.4 mbar, 200 W, 1 min	Not measurable
Air, 0.4 mbar, 200 W, 3 min	270 Ω /sq
Air, 0.4 mbar, 200 W, 5 min	170 Ω /sq

Air, 0.4 mbar, 200 W, 10 min	225 Ω /sq
---------------------------------	------------------



Supplementary Figure 8. Free-standing NPGF. (a) Free-standing NPGF in acetone. PMMA that has not been completely etched during the plasma treatment is dissolved in acetone, and NPGF was lifted off from the Si substrate. (b) 3 μ m-thick PMMA was spin coated on NPGF on Si substrate. This sample was immersed in KOH solution (28.5 %) for a minute and rinsed in deionized water, repeatedly, until the film completely lifts-off. Spin-coated PMMA serves as a supporting layer to stabilize NPGF.